



## Photoacoustic Tomography: In Vivo Imaging from Organelles to Organs

Lihong V. Wang, *et al.*  
*Science* **335**, 1458 (2012);  
DOI: 10.1126/science.1216210

*This copy is for your personal, non-commercial use only.*

If you wish to distribute this article to others, you can order high-quality copies for your colleagues, clients, or customers by [clicking here](#).

Permission to republish or repurpose articles or portions of articles can be obtained by following the guidelines [here](#).

**The following resources related to this article are available online at [www.sciencemag.org](http://www.sciencemag.org) (this information is current as of March 22, 2012):**

**Updated information and services**, including high-resolution figures, can be found in the online version of this article at:

<http://www.sciencemag.org/content/335/6075/1458.full.html>

This article **cites 52 articles**, 3 of which can be accessed free:

<http://www.sciencemag.org/content/335/6075/1458.full.html#ref-list-1>

This article appears in the following **subject collections**:

Physics

<http://www.sciencemag.org/cgi/collection/physics>

# Photoacoustic Tomography: In Vivo Imaging from Organelles to Organs

Lihong V. Wang\* and Song Hu

Photoacoustic tomography (PAT) can create multiscale multicontrast images of living biological structures ranging from organelles to organs. This emerging technology overcomes the high degree of scattering of optical photons in biological tissue by making use of the photoacoustic effect. Light absorption by molecules creates a thermally induced pressure jump that launches ultrasonic waves, which are received by acoustic detectors to form images. Different implementations of PAT allow the spatial resolution to be scaled with the desired imaging depth in tissue while a high depth-to-resolution ratio is maintained. As a rule of thumb, the achievable spatial resolution is on the order of 1/200 of the desired imaging depth, which can reach up to 7 centimeters. PAT provides anatomical, functional, metabolic, molecular, and genetic contrasts of vasculature, hemodynamics, oxygen metabolism, biomarkers, and gene expression. We review the state of the art of PAT for both biological and clinical studies and discuss future prospects.

Optical imaging of tissue offers potential advantages in distinguishing different structures according to their chemical composition. Because tissue is a highly scattering medium for electromagnetic waves in the optical spectral range, methods that attempt to form images from light passing through tissue fall into two categories—ballistic (minimally scattered) optical microscopy and diffuse (multiscattered) optical tomography. The former provides fine resolution but with a low imaging depth in tissue—up to ~1 mm, as defined by the optical diffusion limit (1, 2). When incident photons reach this limit, most of them have undergone tens of scattering events, which scramble the photon paths and inhibit effective optical focusing. In contrast, diffuse optical tomography can probe centimeters into tissue but with poor spatial resolution—equal to about one-third of the imaging depth (3). Randomized paths of the diffuse photons render the image reconstruction mathematically ill-posed. It remains a challenge for pure optical imaging to attain fine spatial resolution at depths beyond the optical diffusion limit.

Fortunately, photons in tissue can be converted into ultrasonic waves, which are scattered much less. Absorption of photons by biomolecules thermoelastically induces pressure waves through the photoacoustic effect. Photoacoustic tomography (PAT) forms images by detecting the induced pressure waves. The conversion from optical to ultrasonic energy immediately brings several advantages: (i) PAT breaks through the optical diffusion limit (4) by capitalizing on the low acoustic scattering in tissue—about three orders of magnitude less than optical scattering in tissue per unit path length. (ii) PAT enables multiscale high-resolution imaging of biological structures, ranging in size from organelles to organs,

using the same contrast. (iii) By exciting different molecules at different optical wavelengths, PAT reveals rich optical contrasts according to chemical composition. (iv) PAT images optical absorption with 100% sensitivity (5), two orders of magnitude greater than those of confocal microscopy and optical coherence tomography (6). (v) PAT provides inherently background-free detection because the photoacoustic amplitude is proportional to the optical absorption; nonabsorbing tissue components present no background. (vi) Unlike fluorescence imaging, PAT ensures no leakage of excitation photons into detectors. (vii) Unlike optical coherence tomography and ultrasonography, PAT is speckle-free (7). (viii) All molecules are optically absorbing at some wavelengths and can potentially be imaged by PAT, whereas far fewer molecules are fluorescent. Although both conventional ultrasound imaging and PAT are based on ultrasonic detection, the former measures only mechanical contrasts and the latter optical and thermoelastic contrasts.

PAT has been developed rapidly in the past decade, with applications explored in vascular biology (8, 9), oncology (10, 11), neurology (12–14), ophthalmology (15, 16), dermatology (17, 18), gastroenterology (19, 20), and cardiology (21, 22). Here, we first introduce the fundamentals and three state-of-the-art embodiments of PAT. Next, we highlight the scalability of PAT over four major length scales in biology—covering organelles, cells, tissues, and organs—and show rich photoacoustic contrasts for tissue anatomies and functions as well as for metabolic, molecular, and genetic processes. To conclude, we envision high-impact applications in biomedicine and point out remaining major challenges in PAT.

## Fundamentals and Major Implementations

PAT is based on optical excitation and ultrasonic detection. The biological tissue to be imaged is irradiated usually by a nanosecond-pulsed laser beam to engender thermal and acoustic impulse responses. The temporally confined optical

absorption induces a temperature rise  $\Delta T$  and consequently an initial pressure rise  $p_0$  due to thermoelastic expansion:  $p_0 = \beta \Delta T / \kappa$ , where  $\beta$  is the thermal expansion coefficient and  $\kappa$  is the isothermal compressibility. Approximately, a temperature rise of 1 mK results in a pressure rise of 800 Pa, which is above the noise level of a typical ultrasonic transducer. As  $\beta$  and  $\kappa$  are beyond our control, it is fortunate that PAT can provide a high signal-to-noise ratio without thermally damaging the tissue. After propagating through the tissue, the pressure wave is detected by an ultrasonic transducer (or a set of transducers) to form a high-resolution tomographic image of optical absorption. Although pulsed lasers are most commonly used, intensity-modulated light sources may be used alternatively (23). Currently, PAT has three major implementations: focused-scanning photoacoustic microscopy (PAM), photoacoustic computed tomography (PACT), and photoacoustic endoscopy (PAE). Whereas PAM and PAE usually aim to image millimeters deep at micrometer-scale resolution, PACT can be implemented for both microscopic and macroscopic imaging.

In PAM, both the optical excitation and ultrasonic detection are focused, and the dual foci are usually configured confocally to maximize sensitivity. Each laser pulse produces a one-dimensional (1D) depth-resolved image without mechanical scanning, and 2D transverse scanning generates a 3D image. The axial resolution is determined by the acoustic time of flight, whereas the lateral resolution is determined by the overlap of the dual foci. Quantitatively, the axial and lateral resolutions are defined as the corresponding full widths at half maximum of the system response to a point target. Depending on whether the optical or ultrasonic focus is finer, PAM is further classified into optical-resolution PAM (OR-PAM) (24, 25) and acoustic-resolution PAM (AR-PAM) (26).

OR-PAM provides lateral resolution at the subcellular or cellular scale ranging from a few hundred nanometers to a few micrometers (Fig. 1A). If such resolution were to be achieved acoustically, the center frequency of the acoustic signal would have to be at least 300 MHz. At such a high frequency, ultrasonic waves sustain severe propagation loss and can penetrate only a few hundred micrometers in tissue. Fortunately, optical focusing can readily confine the photoacoustic excitation for high lateral resolution while maintaining substantial imaging depth; in addition, acoustic focusing can improve detection sensitivity. This system enables in vivo label-free functional imaging of hemoglobin oxygen saturation ( $sO_2$ ) in vessels down to single capillaries (Fig. 1A). However, the imaging depth is limited by optical diffusion to 1.2 mm in vivo (24).

In OR-PAM (Fig. 1A), the laser beam is focused by a microscope objective to a diffraction-limited spot for excitation in the tissue. An optical-acoustic beam combiner, consisting of two prisms sandwiching a thin layer of silicone oil, is positioned beneath the objective to align the optical

Optical Imaging Laboratory, Department of Biomedical Engineering, Washington University, St. Louis, MO 63130, USA.

\*To whom correspondence should be addressed. E-mail: lhwang@wustl.edu

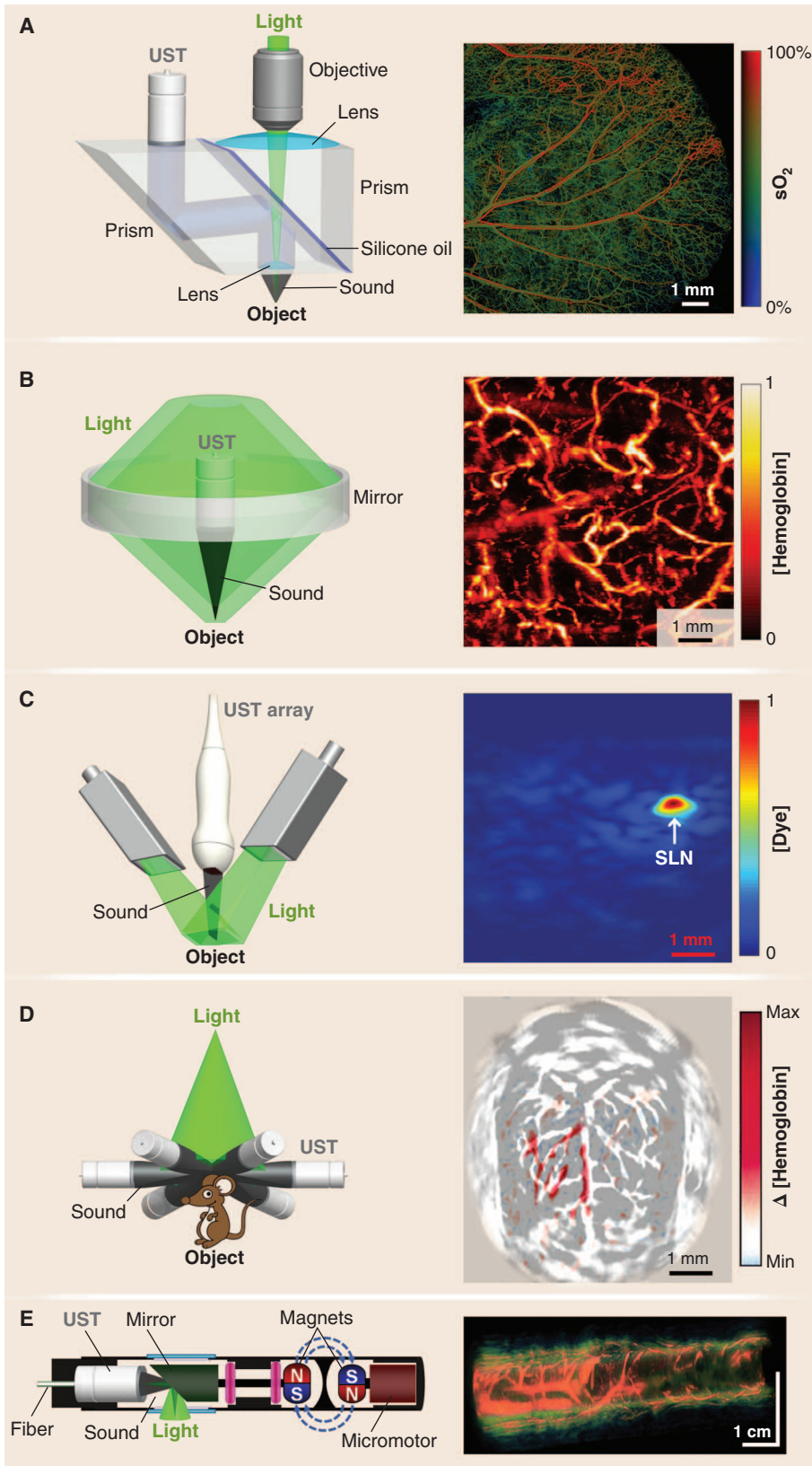


**Fig. 1.** Major embodiments of PAT, with representative in vivo images. **(A)** OR-PAM of  $sO_2$  in a mouse ear. **(B)** AR-PAM of normalized total hemoglobin concentration, [hemoglobin], in a human palm. **(C)** Linear-array PACT of normalized Methylene Blue concentration, [dye], in a rat sentinel lymph node (SLN). **(D)** Circular-array PACT of cerebral hemodynamic changes,  $\Delta$ [hemoglobin], in response to one-sided whisker stimulation in a rat. **(E)** PAE of a rabbit esophagus and adjacent internal organs, including the trachea and lung. UST, ultrasonic transducer.

excitation and acoustic detection coaxially and confocally. The matched optical refractive indices but mismatched acoustic impedances between the prism glass and silicone oil provide optical transmission but acoustic reflection. The optical aberration created by the beam combiner is offset by a correction lens attached to the top surface of the right-angle prism. To focus acoustic detection, a concave acoustic lens is ground into the bottom of the rhomboid prism. An unfocused ultrasonic transducer with a broad bandwidth matching that of the received acoustic waves is attached to the top of the rhomboid prism. Although ideal for light transmission, the solid-liquid interface adversely transforms 85% of the incident acoustic energy from longitudinal waves to shear waves. Because shear waves are not detected with high sensitivity, the rhomboid prism is used to regain the longitudinal wave at the second inclined surface.

At depths beyond the optical diffusion limit and up to a few millimeters, AR-PAM achieves high resolution by taking advantage of the much lower acoustic scattering. Despite diffuse optical excitation, lateral resolution of tens of micrometers is achieved by diffraction-limited acoustic detection. In AR-PAM, optical excitation is implemented through dark-field illumination, as shown in Fig. 1B, for two critical reasons: First, the donut-shaped illumination eliminates otherwise dominant interference signals from the tissue surface. Second, the donut hole is ideal for positioning the ultrasonic transducer coaxially and confocally with respect to the optical excitation. The system provides a 45- $\mu$ m lateral resolution in vivo with a 3-mm imaging depth. Anatomical images of the human cutaneous microvasculature in both the superficial epidermis and deep dermis have been acquired by detecting hemoglobin (Fig. 1B) (18). However, further advancement of the imaging depth to centimeters for macroscopic imaging requires the use of more energetic lasers at low pulse repetition rates. As a result, the transverse scanning becomes too slow for many clinical applications.

To accelerate data acquisition, state-of-the-art ultrasonic array detectors have been used for PACT. The entire region of interest (ROI) is excited by an expanded optical beam, and the photoacoustic waves are simultaneously detected by an ultrasonic array. Then, an inverse algorithm—essentially a method for sophisticated triangulation of photoacoustic sources from the time-resolved acoustic signals—is used to reconstruct a high-resolution image (27–30). As most ultrasonic arrays are 1D, the 2D resolutions in the imaging plane are derived from reconstruction, whereas the orthogonal resolution comes from cylindrical acoustic focusing. The imaging plane can be further translated along the orthogonal dimension for 3D imaging. According to the anatomy of the organ of interest, the ultrasonic array may be configured linearly (31) or circularly (32–34).

In linear-array PACT (Fig. 1C), a multimode optical fiber bundle is bifurcated to flank the handheld

ultrasonic array for dark-field optical illumination, as in AR-PAM. A single laser pulse—with a safe exposure to the tissue ( $\leq 20$  mJ/cm<sup>2</sup> in the visible spectral range)—yields a 2D image. A clinical ultrasound imaging system has been adapted for concurrent imaging with PACT. This system, with an axial resolution of 400  $\mu$ m and a lateral resolution of  $\sim 1$  mm (35), has been used for non-invasive in vivo functional imaging of Methylene Blue-labeled sentinel lymph nodes in small animals (Fig. 1C) (10), and more recently in human breast cancer patients (36).

Circular-array PACT (Fig. 1D) is designed to accommodate round objects, such as the brain, a peripheral joint, and even the whole body of a small animal. The ROI is encircled by the array to detect photoacoustic waves propagating along all in-plane directions; unlike the partial-view detection (i.e., the angle subtended by the ultrasound detectors with respect to the object is less than 360°) in linear-array PACT, full-view detection provides high-quality images without missing boundaries (37). The principle of circular-array PACT was originally demonstrated by circularly scanning a single-element ultrasonic transducer in the first functional PAT system, which imaged the cerebral vascular response to one-sided whisker stimulation in an adult rat through intact scalp and skull with an in-plane resolution of  $\sim 200$   $\mu$ m (Fig. 1D) (14).

PAE has been intensively investigated in recent years (19–22, 38) as a means of imaging internal organs such as the esophagus and colon. In a representative PAE design (Fig. 1E) (19), light from a high-repetition-rate laser is delivered by a multimode optical fiber placed in the central hole of a ring transducer. An optically and acoustically reflective mirror, driven by a micromotor through coupled magnets, rotates both the optical illumination and the acoustic detection for circumferential cross-sectional scanning. Further, a linear motor pulls back the entire probe for volumetric imaging. In contrast to conventional optical endoscopy, which has an imaging depth within the optical diffusion limit, PAE has shown a 7-mm imaging depth in the dorsal region of a rat colon ex vivo (Fig. 1E) (20).

### Multiscale PAT in Vivo: Organelles, Cells, Tissues, and Organs

The elegant marriage between light and sound endows PAT with the unique capability of scaling its spatial resolution and imaging depth across both optical and ultrasonic dimensions. The lateral resolution of OR-PAM is given by  $R_{L,OR} = 0.51 \cdot \lambda / NA$ , where  $\lambda$  denotes the optical wavelength and NA is the numerical aperture of the microscope objective. Varying the NA can scale the lateral resolution from subwavelength to a few wavelengths, with the imaging depth varied accordingly. With NA = 1.23 and  $\lambda = 532$  nm, a 220-nm lateral resolution has been achieved with an imaging depth of 100  $\mu$ m, enabling in vivo subcellular imaging of individual melanosomes (Fig. 2A) (39). Halving the NA to 0.63 quad-

riples the imaging depth while the lateral resolution is still maintained at 500 nm (40). Reducing the NA to 0.1 further triples the imaging depth to the optical diffusion limit and relaxes the lateral resolution to 2.6  $\mu$ m, enabling in vivo label-free functional imaging of individual red blood cells flowing in capillaries (Fig. 2B) (24). As in conventional optical microscopes, it is possible to combine multiple optical objectives of different NAs in a single OR-PAM system, which would allow convenient adjustment of the magnification. Further, OR-PAM and AR-PAM systems can be integrated to extend the range of scalability of a single device.

The lateral resolution of AR-PAM or partial-view PACT is given by  $R_{L,AR} = 0.71 \cdot v_s / (NA \cdot f_0)$ ,

within the resolving power of human eyes, such an instrument is called a photoacoustic microscope (PAMac). A PACT system based on a clinical linear ultrasound array operating with a frequency band of 4 to 8 MHz has extended the imaging depth to 7 cm, with a submillimeter lateral resolution (720  $\mu$ m) (36). Figure 2D shows a representative in vivo PACT image of the breast vasculature in a human volunteer (33). PACT can also perform microscopic imaging when operating at high ultrasonic frequencies (42).

The axial resolution of PAM or partial-view PACT always originates from the time of arrival of the acoustic signal. It can be estimated as  $R_A = 0.88 \cdot v_s / \Delta f$ , where  $\Delta f$  is the photoacoustic bandwidth (approximately proportional to  $f_0$ ). So far,

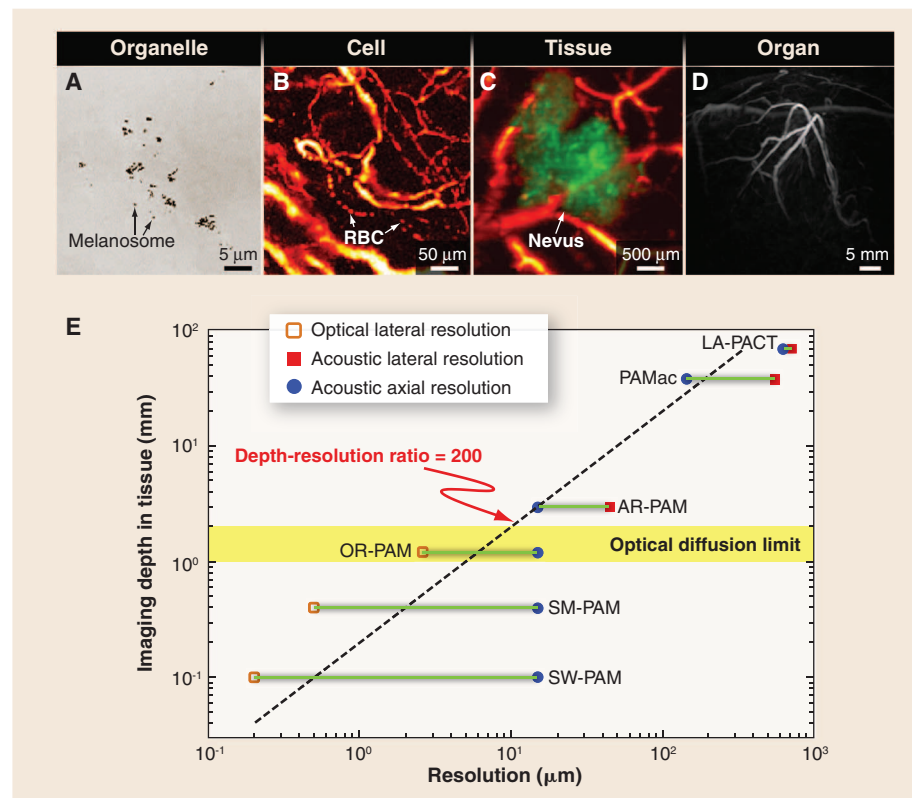


**Fig. 2.** Multiscale PAT of organelles, cells, tissues, and organs in vivo. (A) Subwavelength (SW) PAM of melanosomes in the ear of a black mouse. (B) OR-PAM of individual red blood cells traveling along a capillary in a mouse ear. (C) AR-PAM of a nevus on a human forearm. (D) PACT of a human breast. (E) Imaging depth versus spatial resolution in PAT. SM, submicrometer; LA, linear array.

where  $v_s$  is the speed of sound, NA is the acoustic numerical aperture, and  $f_0$  is the photoacoustic center frequency. The center frequency  $f_0$  is determined by the laser pulse width, the targeted tissue depth, and the ultrasonic transducer's frequency response. With  $f_0 = 50$  MHz and NA = 0.44, AR-PAM has achieved a lateral resolution of 45  $\mu$ m and an imaging depth of 3 mm (26). Such a system is adequate to see through human skin lesions in vivo, as required for accurate diagnosis and staging (Fig. 2C) (18). Reducing the center frequency to 5 MHz extends the imaging depth to 4 cm and relaxes the lateral resolution to 560  $\mu$ m (41). Because the resolution is now

axial resolutions ranging from 15 to 640  $\mu$ m have been achieved in PAT systems of various targeted imaging depths (25, 36). The 2D in-plane resolutions of full-view PACT can be similarly estimated with  $\Delta f$ .

Figure 2E summarizes the scalability of PAT. Within the optical diffusion limit, the imaging depth of OR-PAM is approximately proportional to the chosen lateral resolution. Beyond the limit, the imaging depth is primarily determined by the frequency-dependent acoustic attenuation. As both  $f_0$  and  $\Delta f$  are inversely proportional to the desired imaging depth, the lateral and axial resolutions are proportional to the imaging depth. For both

regimes, the ratio of the imaging depth to the best spatial resolution is roughly a constant of 200 (as shown by the slope of the dashed line in Fig. 2E), making PAT a high-resolution modality across all four length scales. The optimal tradeoff between spatial resolution and imaging depth depends on the application.

### Multicontrast PAT in Vivo: Anatomy, Function, Metabolism, and Molecular/Genetic Processes

With selected optical wavelengths, PAT can probe a wide variety of endogenous or exogenous absorbers to reveal the anatomy, function, metabolism, and molecular/genetic processes in biological systems in vivo. Endogenously, DNA/RNA, hemoglobin, melanin, water, and lipid are important anatomical and functional contrast agents. Using the strong ultraviolet absorption of DNA and RNA, OR-PAM recently achieved noninvasive imaging of individual cell nuclei (Fig. 3A), which can provide an in vivo label-free substitute for ex vivo hematoxylin and eosin staining histology (43). Because malfunction of DNA replication induces abnormal nuclear morphology in cancer, this technology can potentially provide early detection and intraoperative demarcation of cancer. Hemoglobin, as a primary oxygen carrier, is essential to tissue metabolism. Using hemoglobin's predominant optical absorption in the visible range over other absorbers, PAT provides comprehensive anatomical and functional imaging of the blood circulation system (8, 44). Abnormal concentrations of water and lipid can be important disease indicators. Their relatively strong optical absorption in the near-infrared range allows PAT to map their distributions at substantial depths in vivo (45, 46). Melanin, a major pigment in the skin and most melanomas, has broadband optical absorption from the ultraviolet to the near-infrared range, which can be spectroscopically distinguished from hemoglobin absorption by PAT. Simultaneous imaging of the melanoma anatomy and the surrounding vascular function provides an unprecedented opportunity for understanding the interactions between a tumor and its microenvironment and for noninvasively detecting and staging melanoma (Fig. 3B) (26).

Exogenous contrast agents further extend PAT to molecular and genetic imaging. Nanoparticles, organic dyes, and reporter gene products can be excellent photoacoustic contrast agents. The primary advantage of gold nanoparticles lies in their large absorption cross section tuned to the optical window (~730 nm), minimizing endogenous absorption and maximizing imaging depth. Moreover, the bioconjugation capability of nanoparticles enables effective biomarker targeting for both molecular imaging (Fig. 3, C and D) (11, 47) and drug delivery. Recently, the use of iron oxide and gold-coupled core-shell nanoparticles as a photoacoustic contrast agent has led to the development of magnetomotive PAT (Fig. 3E) (48), which markedly improves the contrast and specificity of PAT by suppressing the nonmagneto-

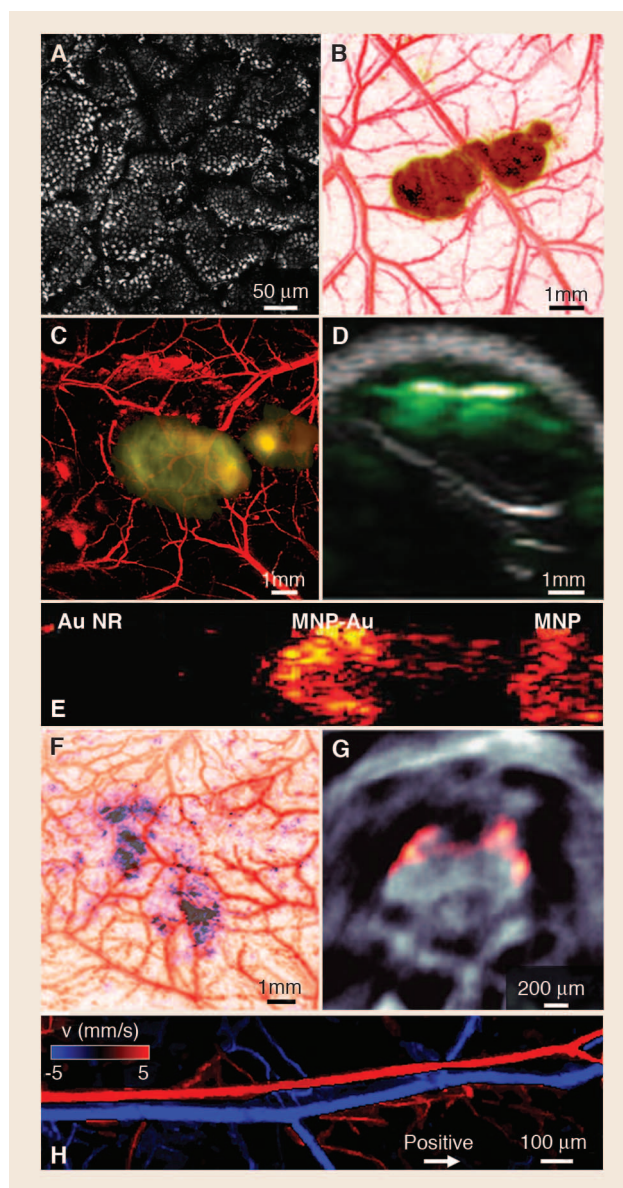


**Fig. 3.** Multicontrast PAT of tissue anatomy, function, molecular biomarkers, and gene expression. (A) OR-PAM of epithelial cell nuclei in the intestinal villi of a mouse ex vivo by excitation of DNA and RNA. (B) AR-PAM of a subcutaneously inoculated B16 melanoma and the surrounding vasculature on the back of a living mouse. (C) AR-PAM of a subcutaneously inoculated B16 melanoma labeled with targeted gold nanocages on the back of a living mouse. (D) Dual-contrast ultrasound (gray) and photoacoustic (green) imaging of a tumor labeled with single-walled carbon nanotubes in a living mouse. (E) Magnetomotive PAT of a polyvinyl alcohol phantom with three inclusions, each 2 mm in diameter. The left inclusion contains gold nanorods (Au NR) with absorption comparable to the 3 nM magnetic-gold hybrid nanoparticles (MNP-Au) placed in the center inclusion, and the right inclusion contains 3 nM magnetic nanoparticles (MNP). (F) AR-PAM of a lacZ-marked 9L gliosarcoma and the surrounding vasculature under the scalp of a living rat. (G) PACT of the brain of a 6-month-old mCherry-expressing transgenic zebrafish. (H) OR-PAM of blood flow velocity and direction in the ear of a living mouse.

motive background. Depending on the application, the relatively slow tissue clearance of nanoparticles can be either an advantage or a disadvantage.

Although the clinical translation of most nanoparticles is still awaiting FDA approval, many organic dyes have been approved for human use. Organic dyes clear rapidly from the body because of their small molecular size (typically ~1 nm), and some can penetrate the blood-brain barrier. Reporter gene products can be detected for PAT of biological processes at the genetic level, as was demonstrated using the *LacZ* gene—a common reporter encoding the protein  $\beta$ -galactosidase (49). Gliosarcoma cells transfected with *LacZ* genes were inoculated into a Sprague-Dawley rat. As the tumor grew, *LacZ* genes were expressed to  $\beta$ -galactosidase, which metabolized the locally injected lactose-like substrate into highly absorbing blue products, thereby providing contrast for genetic PAT in vivo (Fig. 3F) (49). Even fluo-

rescent proteins from reporter genes have been imaged in vivo by PAT (Fig. 3G) (50).

All molecules can potentially be imaged by PAT at appropriate wavelengths, whereas only a small subset of molecules is fluorescent. Even fluorophores can serve as absorbing contrast agents for PAT (13, 50, 51). Optical excitation of fluorophores, in the absence of photochemical relaxation, relaxes via either fluorescence or thermal emission. Because most fluorophores have imperfect fluorescence quantum yields, PAT can rely on the thermal relaxation for high-resolution deep imaging of fluorophores.

Besides the aforementioned static contrasts, PAT can also image two important dynamic contrasts: blood flow (hemodynamic contrast) and temperature variation (thermodynamic contrast). The recently discovered photoacoustic Doppler effect laid the foundation for PAT of flow (52). Figure 3H shows a functional PAT image of both blood flow velocity and direction in a living

mouse (53). With excellent scalability, Doppler PAT bridges the spatial gap between scattering-based optical and ultrasonic technologies. More important, the high optical absorption contrast between the intravascular blood and extravascular background greatly increases detection sensitivity.

Tissue temperature monitoring is essential for thermal therapy. Because the initial photoacoustic pressure depends on the equilibrium temperature, PAT provides a potential means for high-resolution temperature imaging deep in tissue (54, 55). Recent tissue phantom experiments showed that the initial photoacoustic pressure increases with the equilibrium temperature by ~5% per degree, which enables a sensitivity of the order of 0.1°C (54).

Combining both static and dynamic contrasts from PAT enables metabolic imaging. Indeed, PAT is the only modality that uses endogenous contrasts to measure all the parameters—including vessel diameter, total hemoglobin concentration,  $\text{SO}_2$ , tissue volume of interest, and blood flow velocity—required to compute the metabolic rate of oxygen ( $\text{MRO}_2$ ). Recently, label-free absolute quantification of the  $\text{MRO}_2$  in a living mouse was demonstrated (44).

## Outlook

PAT is expected to find broad applications in biology and medicine. Major preclinical applications include imaging of angiogenesis, microcirculation, tumor microenvironments, drug response, brain functions, biomarkers, and gene activities. Initial clinical applications include melanoma cancer imaging, gastrointestinal tract endoscopy, intravascular catheter imaging, neonatal brain imaging, breast cancer detection, prostate cancer detection, guided sentinel lymph node needle biopsy for cancer staging, early chemotherapeutic response imaging, dosimetry in thermal therapy, in vivo label-free histology, blood perfusion imaging, blood oxygenation imaging, and tissue metabolism imaging. Although preclinical PAT systems have been commercialized, clinical systems need to pass rigorous validation and arduous regulatory approval.

PAT is distinctly capable of in vivo metabolic imaging based only on endogenous contrast. Upscaling metabolic PAT from small animals (44) to humans is expected to revolutionize the screening, diagnosis, and treatment of metabolic diseases, particularly cancers and cerebral disorders. Downscaling metabolic PAT to cells provides a tool for understanding metabolic pathways. Because hypermetabolism is a quintessential hallmark of cancer, metabolic PAT may enable in vivo cancer screening at the earliest stage without using exogenous contrast agents.

The scalability of PAT provides an unprecedented opportunity to link a complex biological system at multiple length scales through consistent optical absorption contrasts. In current practice, microscopic biological structures (including organelles and cells) are usually imaged by optical microscopy, whereas macroscopic

structures (including tissues and organs) are imaged using nonoptical modalities such as x-ray computed tomography. Correlation of microscopic and macroscopic images can be challenging because of their vastly different contrast mechanisms. Imaging with the same contrast enables PAT to bridge this gap between the microscopic and macroscopic domains. Therefore, experimental observations from multiscale PAT are expected to facilitate the development of theoretical models for systems biology that explain and even predict biological phenomena at multiple scales. Moreover, PAT will likely accelerate the translation of microscopic laboratory discoveries to macroscopic clinical practice.

PAT still must overcome multiple technical challenges to maximize its impact in biomedicine. For high-speed multicontrast PAM or PAE based on spectroscopy, high-repetition lasers with fast wavelength-tuning at each scan position must be developed. PAE probes require further miniaturization to fit within generic endoscopes or even intravascular catheters. For deep-penetrating PACT, high-energy lasers with video-rate pulse repetition are needed. The required laser energy, however, can potentially be lowered by using time-reversed ultrasonically encoded (TRUE) optical focusing to improve light penetration (56). Also needed are sophisticated algorithms to perfect molecular quantification and to suppress skull-induced artifacts. It is anticipated that further advancement of this fast-growing imaging technology will revolutionize both fundamental life sciences and clinical patient care.

## References and Notes

1. L. V. Wang, H. Wu, *Biomedical Optics: Principles and Imaging* (Wiley, Hoboken, NJ, 2007).
2. The optical diffusion limit represents the depth of the quasi-ballistic regime in biological tissue beyond which light propagating along the predefined linear trajectory becomes too weak to be detected in practice. It is usually equated with the transport mean free path (i.e., the mean distance between two consecutive equivalent isotropic scattering events).
3. J. P. Culver, V. Ntziachristos, M. J. Holboke, A. G. Yodh, *Opt. Lett.* **26**, 701 (2001).
4. L. V. Wang, *Nat. Photonics* **3**, 503 (2009).
5. The sensitivity is defined here as the ratio of the fractional change in the photoacoustic signal to the fractional change in the optical absorption coefficient.
6. L. V. Wang, *IEEE J. Sel. Top. Quantum Electron.* **14**, 171 (2008).
7. Z. Guo, L. Li, L. V. Wang, *Med. Phys.* **36**, 4084 (2009).
8. S. Oladipupo *et al.*, *Proc. Natl. Acad. Sci. U.S.A.* **108**, 13264 (2011).
9. S. S. Oladipupo *et al.*, *Blood* **117**, 4142 (2011).
10. T. N. Erpelding *et al.*, *Radiology* **256**, 102 (2010).
11. C. Kim *et al.*, *ACS Nano* **4**, 4559 (2010).
12. S. Hu, L. V. Wang, *Front. Neuroenerg.* **2**, (2010).
13. S. Hu, P. Yan, K. Maslov, J.-M. Lee, L. V. Wang, *Opt. Lett.* **34**, 3899 (2009).
14. X. Wang *et al.*, *Nat. Biotechnol.* **21**, 803 (2003).
15. S. Hu, B. Rao, K. Maslov, L. V. Wang, *Opt. Lett.* **35**, 1 (2010).
16. S. Jiao *et al.*, *Opt. Express* **18**, 3967 (2010).
17. E. Z. Zhang *et al.*, *Biomed. Opt. Express* **2**, 2202 (2011).
18. C. P. Favazza, O. Jassim, L. A. Cornelius, L. V. Wang, *J. Biomed. Opt.* **16**, 016015 (2011).

19. J.-M. Yang *et al.*, *Opt. Lett.* **34**, 1591 (2009).
20. J.-M. Yang *et al.*, *Proc. SPIE* **8223**, 822316 (2012).
21. K. Jansen, A. F. W. van der Steen, H. M. M. van Beusekom, J. W. Oosterhuis, G. van Soest, *Opt. Lett.* **36**, 597 (2011).
22. B. Wang *et al.*, *Nano Lett.* **9**, 2212 (2008).
23. K. Maslov, L. V. Wang, *J. Biomed. Opt.* **13**, 024006 (2008).
24. S. Hu, K. Maslov, L. V. Wang, *Opt. Lett.* **36**, 1134 (2011).
25. K. Maslov, H. F. Zhang, S. Hu, L. V. Wang, *Opt. Lett.* **33**, 929 (2008).
26. H. F. Zhang, K. Maslov, G. Stoica, L. V. Wang, *Nat. Biotechnol.* **24**, 848 (2006).
27. K. P. Kostli *et al.*, *IEEE J. Sel. Top. Quantum Electron.* **7**, 918 (2001).
28. M. Xu, L. V. Wang, *IEEE Trans. Med. Imaging* **21**, 814 (2002).
29. D. Finch, S. K. Patch, *SIAM J. Math. Anal.* **35**, 1213 (2003).
30. M. Xu, L. V. Wang, *Phys. Rev. E* **71**, 016706 (2005).
31. R. J. Zemp *et al.*, *J. Biomed. Opt.* **12**, 010501 (2007).
32. H. P. Brecht *et al.*, *J. Biomed. Opt.* **14**, 064007 (2009).
33. R. A. Kruger, R. B. Lam, D. R. Reinecke, S. P. Del Rio, R. P. Doyle, *Med. Phys.* **37**, 6096 (2010).
34. C. Li *et al.*, *J. Biomed. Opt.* **15**, 010509 (2010).
35. C. Kim, T. N. Erpelding, L. Jankovic, M. D. Pashley, L. V. Wang, *Biomed. Opt. Express* **1**, 278 (2010).
36. L. V. Wang, seminar presented at the Isaac Newton Institute for Mathematical Sciences: Inverse Problems, Cambridge, 23 August 2011; [www.newton.ac.uk/programmes/INV/seminars/082314051.html](http://www.newton.ac.uk/programmes/INV/seminars/082314051.html).
37. Y. Xu, L. V. Wang, G. Ambartsoumian, P. Kuchment, *Med. Phys.* **31**, 724 (2004).
38. Y. Yang *et al.*, *Biomed. Opt. Express* **2**, 2551 (2011).
39. C. Zhang, K. Maslov, L. V. Wang, *Opt. Lett.* **35**, 3195 (2010).
40. C. Zhang *et al.*, *J. Biomed. Opt.* **17**, 020501 (2012).
41. K. H. Song, L. V. Wang, *J. Biomed. Opt.* **12**, 060503 (2007).
42. L. Song, K. Maslov, L. V. Wang, *Opt. Lett.* **36**, 1236 (2011).
43. D. K. Yao, K. Maslov, K. K. Shung, Q. Zhou, L. V. Wang, *Opt. Lett.* **35**, 4139 (2010).
44. J. Yao, K. I. Maslov, Y. Zhang, Y. Xia, L. V. Wang, *J. Biomed. Opt.* **16**, 076003 (2011).
45. Z. Xu, Q. Zhu, L. V. Wang, *J. Biomed. Opt.* **16**, 066020 (2011).
46. H. W. Wang *et al.*, *Phys. Rev. Lett.* **106**, 238106 (2011).
47. A. De la Zerda *et al.*, *Nat. Nanotechnol.* **3**, 557 (2008).
48. Y. Jin, C. Jia, S. W. Huang, M. O'Donnell, X. Gao, *Nat. Commun.* **1**, 41 (2010).
49. L. Li, H. F. Zhang, R. J. Zemp, K. Maslov, L. V. Wang, *J. Innov. Opt. Health Sci.* **1**, 207 (2008).
50. D. Razansky *et al.*, *Nat. Photonics* **3**, 412 (2009).
51. D. Razansky, C. Vinegoni, V. Ntziachristos, *Opt. Lett.* **32**, 2891 (2007).
52. H. Fang, K. Maslov, L. V. Wang, *Phys. Rev. Lett.* **99**, 184501 (2007).
53. J. Yao, K. I. Maslov, Y. Shi, L. A. Taber, L. V. Wang, *Opt. Lett.* **35**, 1419 (2010).
54. M. Pramanik, L. V. Wang, *J. Biomed. Opt.* **14**, 054024 (2009).
55. J. Shah *et al.*, *J. Biomed. Opt.* **13**, 034024 (2008).
56. X. Xu, H. Liu, L. V. Wang, *Nat. Photonics* **5**, 154 (2011).

**Acknowledgments:** We thank J. Ballard for close reading of the manuscript, and J. Yao for providing Fig. 3H. Supported by NIH grants R01 EB000712, R01 EB008085, R01 CA134539, U54 CA136398, R01 CA157277, R01 EB010049, and R01 CA159959. L.V.W. has financial interests in Microphotoacoustics Inc. and Endra Inc., which, however, did not support this work.

10.1126/science.1216210